Letter

Experimental Realization of Acoustic Bianisotropic Gratings

Steven R. Craig,[1] Xiaoshi Su,[2] Andrew Norris,[2] and Chengzhi Shi[1,3,*]

[1] *Meta Acoustics Lab, GWW School of Mechanical Engineering, Georgia Institute of Technology, Atlanta, Georgia 30332, USA*

[2] *Department of Mechanical and Aerospace Engineering, Rutgers University, Piscataway, New Jersey 08854, USA*

[3] *Parker H. Petit Institute for Bioengineering and Biosciences, Georgia Institute of Technology, Atlanta, Georgia 30332, USA*

(Received 30 December 2018; revised manuscript received 3 May 2019; published 6 June 2019)

Acoustic bianisotropic materials couple pressure and local particle velocity fields to simultaneously excite monopole and dipole scattering, which results in asymmetric wave transmission and reflection of airborne sound. We systematically realize an arbitrarily given bianisotropic coupling between the pressure and velocity fields for asymmetric wave propagation by an acoustic grating with inversion symmetry breaking. This acoustic bianisotropic grating is designed by optimizing the unit cells with a finite element method to achieve the desired scattering wavevectors determined by the bianisotropic induced asymmetric wave propagation. The symmetry and Bloch wavevectors in the reciprocal space resulting from the grating are analyzed, which match with the desired scattering wavevectors. The designed structures are fabricated for the experimental demonstration of the bianisotropic properties. The measured results match with the desired asymmetric wave scattering fields.

DOI: 10.1103/PhysRevApplied.11.061002

Manipulating acoustic wave propagation facilitates the development of alternative applications in numerous fields, including lensing [1], noise control [2], and high-intensity focused ultrasound therapies [3,4]. Due to the reversible nature of wave functions, classical acoustic waves propagate with symmetries in both time and space. Asymmetric transmission and reflection stem from breaking these symmetries for the realization of nonreciprocal acoustic propagation, inversion symmetry violation, or parity-time symmetry. A common way to achieve nonreciprocity in acoustics is by altering the frequency of incident waves using nonlinear materials and filtering unwanted frequencies with sonic crystals, enabling one-way acoustic propagation [5]. Using nonlinearities to achieve asymmetric wave propagation has also been demonstrated with active elements by coupling Helmholtz resonators with a piezoelectric material and a nonlinear circuit [6]. Alternative techniques to realize nonreciprocity have been accomplished with circular flow in a resonant ring cavity to introduce a momentum bias on the propagating wave [7]. This is an acoustic analog to the Zeeman Effect in electromagnetics, which is achieved by a magnetic field. Applying this approach of nonreciprocal circular flow to an array of cylindrical sonic crystals leads to the creation of a topologically protected edge state with one-way acoustic wave propagation, which is an acoustic analogy of the quantum Hall effect [8–10]. Besides breaking the time reversal symmetry with circular flow or synthetic angular momentum, topologically protected one-way edge states were also realized by breaking the inversion symmetry of phononic crystals that induces acoustic pseudospin, analogous to the quantum spin Hall effect [11–13]. Generalizing topological acoustics in higher dimensions leads to the exploration of acoustic Weyl points and Fermi arcs, resulting in asymmetric wave propagation in three dimensions [14–16]. In addition, asymmetric wave transmission has been observed in non-Hermitian structures with pure loss effects [17]. Non-Hermitian acoustic structures with parity-time symmetry, where the loss and gain materials were exactly balanced, were demonstrated to exhibit asymmetric wave reflection while maintaining total transmission on both sides of the structure at their exceptional points [18–20].

Bianisotropic materials enable asymmetric wave scattering with unitary efficiency in the bulk state compared to the existing approaches [21]. Bianisotropic properties were observed in electromagnetism where a coupling tensor relates electric and magnetic fields with monopolar and dipolar moments in the scattered waves [22]. Acoustic bianisotropic materials couple the pressure and local particle velocity fields with monopole and dipole scattering resulting in asymmetric wave propagations [23–30]. The bianisotropic material was used as an effective sound barrier [31]. The coupling between the pressure and local

*chengzhi.shi@me.gatech.edu

 © 2019 American Physical Society

particle velocity fields along with the scattered acoustic monopole and dipole is characterized by a polarizability tensor. In a two-dimensional (2D) scenario, the polarizability tensor is a second-order tensor given by

$$\begin{pmatrix} M \\ D_x \\ D_y \end{pmatrix} = \begin{pmatrix} \hat{\alpha}^{pp} & \hat{\alpha}_x^{pv} & \hat{\alpha}_y^{pv} \\ \hat{\alpha}_x^{vp} & \hat{\alpha}_{xx}^{vv} & \hat{\alpha}_{xy}^{vv} \\ \hat{\alpha}_y^{vp} & \hat{\alpha}_{yx}^{vv} & \hat{\alpha}_{yy}^{vv} \end{pmatrix} \begin{pmatrix} p \\ v_x \\ v_y \end{pmatrix}, \quad (1)$$

where M is the monopole scattering, D_x and D_y are the dipole scattering along the x and y axes, p is the pressure field, v_x and v_y are the local particle velocity fields in the x and y directions, and $\hat{\alpha}_j^i$ are the elements of the polarizability tensor with i denoting the coupling between the pressure and local particle velocity fields and j denoting the coupling axes, respectively. Given an arbitrary polarizability tensor, one can obtain the scattering field of a bianisotropic particle [32]. For example, the scattering of a bianisotropic particle allowing for both forward and backward scattering, whose polarizability tensor is a function of frequency given by Fig. 1(a), is obtained in Fig. 1(b). Similarly, the scattering of another bianisotropic particle with a polarizability tensor given by Fig. 1(c) only permitting backwards scattering is shown in Fig. 1(d).

In this work, we aim to realize an acoustic bianisotropic grating with its polarizability tensor given by Fig. 1(a) at 6 kHz (wavelength equal to 5.7 cm). Because the bianisotropic grating we intend to fabricate is linear, the wavelength and frequency remain unchanged during the scattering process, and the incident and scattered wavevectors are retained on a circle with its radius given by $k = 2\pi/\lambda = 109.9\ \mathrm{m}^{-1}$ [Figs. 2(a) and 2(b)]. The Bloch wavevectors of the grating required to achieve this asymmetric wave propagation in Fig. 1(b) are given by the difference between the incident and scattered wavevectors shown by the black arrows in Figs. 2(a) and 2(b). A -45-degree incident wave is completely reflected by the bianisotropic grating back toward the source that requires a Bloch wavevector $(-\sqrt{2}k, \sqrt{2}k)$ given by the structure [Fig. 2(a)]. The time reversal of the scattering process for this incidence is identical to itself [Fig. 2(a)]. On the other hand, a 45-degree incident wave is refracted with a total transmission in the -45-degree direction, which requires a Bloch wavevector $(0, -\sqrt{2}k)$ from the grating shown in Fig. 2(b). The time reversal of this incident case exhibits the same refraction, confirming the preservation of time reversal symmetry in the bianisotropic grating. The asymmetric wave scattering of the -45- and 45-degree incidents reveal the violation of parity symmetry in the y direction, indicating the inversion symmetry breaking of the bianisotropic grating about the x axis. Thus, the mirrored Bloch wavevectors $(\sqrt{2}k, \sqrt{2}k)$ and $(0, \sqrt{2}k)$ about the x axis are not provided by the grating. To realize this bianisotropic grating, we determine the grating periodicity from the scattered wave directions from the aforementioned polarizability tensor. The geometry of the unit cells are optimized based on a finite element method, which maximizes the scattering efficiency of the grating [33]. The resulting bianisotropic grating consists of a periodic array of scatterers along the y axis with a 40.4-mm spacing. Each scatterer consists of a rectangle having a base of 39.5 mm and height of 14.8 mm adjacent to a second rectangle with a 19.5-mm base and 21.2-mm height centered above the first [Fig. 2(c)]. In order to confirm that the grating elements provide the desired scattering in Fig. 1(b), Fourier analysis of the symmetry properties of the scattered wavevectors in the reciprocal space is performed [Fig. 2(d)], which results in the wavevectors required by the scattering in Figs. 2(a) and 2(b).

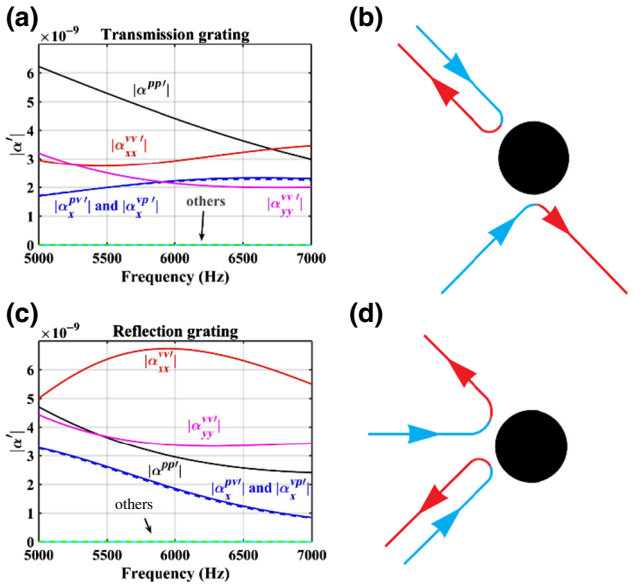

FIG. 1. (a) The elements of the polarizability tensor of a bianisotropic particle that allows both forward and backward scattering as functions of frequency. (b) Asymmetric wave scattering for different incidences from the bianisotropic particle in (a). (c) The elements of the polarizability tensor of a bianisotropic particle with only backward scattering. (d) Asymmetric wave scattering for different incidences from the bianisotropic particle in (c). For both (b) and (d), the blue arrows represent incident and red arrows represent scattered waves, respectively.

To experimentally verify the bianisotropic properties of the designed grating, 25 aluminum grating elements are machined by computer numerical control milling [Fig. 2(e)]. In our experiment, the grating elements are arranged in a 2D waveguide with a height of 2 cm bounded by two 1000 mm by 1500 mm acrylic sheets. Plane waves are generated by a speaker array consisting of twelve 17-mm diameter speakers spaced $\lambda/2$ apart, positioned at a 45-degree angle relative to the grating with the closest edge of the array being 500 mm away from the grating [Fig. 2(e)]. In order to create a consistent signal, the pressure

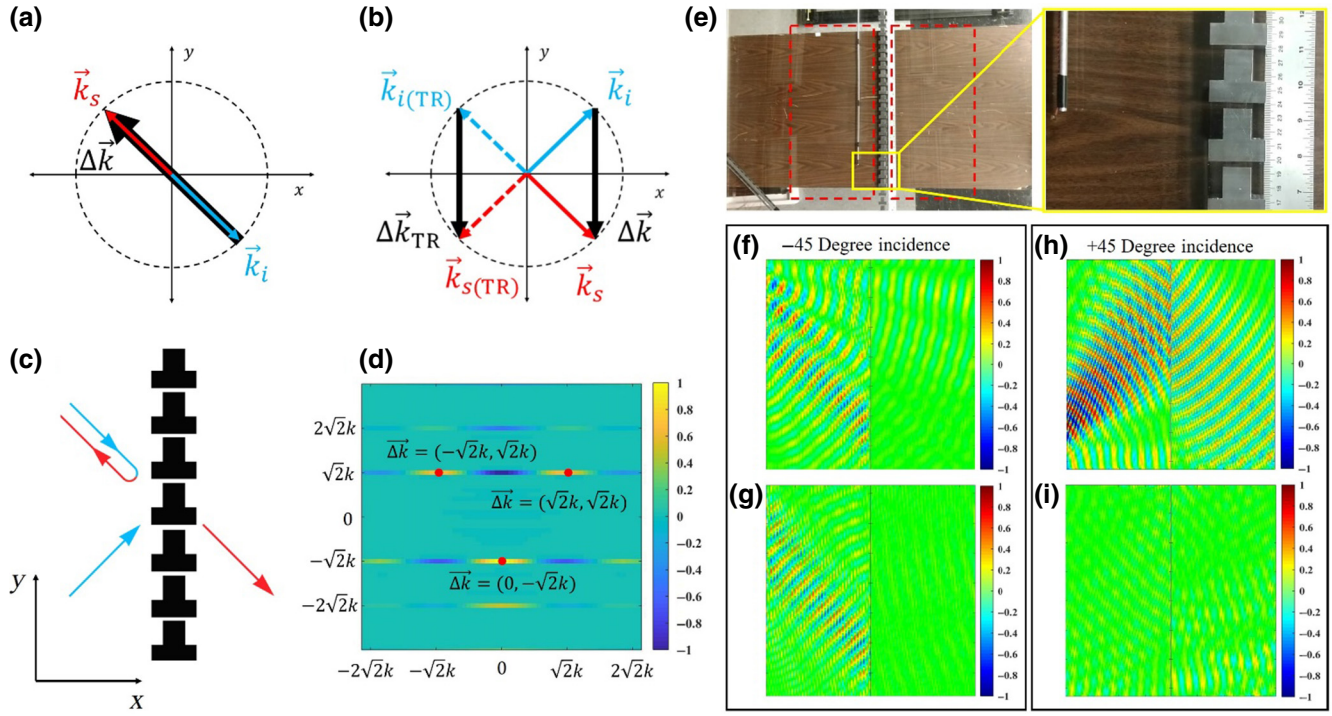

FIG. 2. (a) Wave-grating interaction for the transmission case for −45-degree incidence in the reciprocal space. (b) Wave-grating interaction for +45-degree incidence as well as the time reversed case represented by the dashed lines. For both (a) and (b), the incident, scattered, and Bloch wavevectors are represented by $\vec{k}_i$, $\vec{k}_s$, and Δk, respectively. (c) Bianisotropic grating structure with asymmetric wave scattering in (a) and (b) determined by optimizing the unit cells using a finite element method. (d) 2D spatial Fourier transform of the grating geometry with the expected scattering wavevectors having the highest intensity. (e) Experimental set up for the bianisotropic transmission grating. The enlarged view shows the detailed structure of the grating. The outlined rectangles with red dashed lines represent the scanned areas. (f) Measured pressure field of acoustic waves propagating with positive k_x component for −45-degree incidence. (g) Measured pressure field with negative k_x component for −45-degree incidence. (h) Measured pressure field of acoustic waves propagating with positive k_x component for +45-degree incidence. (i) Measured pressure field with negative k_x component for +45-degree incidence. All the pressure fields in (f), (g), (h), and (i) are normalized by their corresponding maximum amplitude in each measurement.

amplitude of the speakers is controlled by a digital, multichannel recorder while an omnidirectional microphone attached to a motorized positioner measures the pressure fields for both the −45- and 45-degree incidence cases. The motorized positioner is controlled by a MATLAB$^{\mathrm{TR}}$ script to scan two 450 mm by 800 mm areas, which are 10 mm away from the grating with a scan resolution of $\lambda/10$. A lock-in amplifier records the amplitude and phase of the acoustic waves in the scan area [Fig. 2(e)]. To distinguish the incident and scattered waves, spatial 2D Fourier analysis is performed on the measured pressure fields, differentiating the waves with positive k_x [Figs. 2(f) and 2(h)] and negative k_x components [Figs. 2(g) and 2(i)]. For the −45-degree incidence, the acoustic wave is reflected back toward the source by the bianisotropic grating with pressure reflection coefficient $R = 0.72$ and no transmission through the grating [Figs. 2(f) and 2(g)]. This experimental result matches the desired scattering of the bianisotropic structure in Fig. 1(b) with its polarizability tensor given by Fig. 1(a). On the other hand, a 45-degree incidence results in a transmission at a −45-degree angle with pressure transmission coefficient $T = 0.78$ and no reflection from the grating [Figs. 2(h) and 2(i)], which matches the scattering of the bianisotropic material in Fig. 1(b). The full wave simulations show near perfect reflection and transmission for the two incident cases, respectively [33], which indicates near perfect scattering efficiencies. The experimental error arises from the speaker array being an imperfect source that excites unwanted wavevectors. In addition, the finite dimensions of the waveguide possess open boundaries at the edges of the acrylic sheets resulting in unwanted reflections [33]. Further error arises from the fabrication and imperfect alignment of the grating. These experimental results confirm the feasibility for the realization of bianisotropic properties by breaking the inversion symmetry of the structure.

The realization of a bianisotropic grating with polarizability defined by Fig. 1(d) at 6 kHz is similar to the procedure previously executed. By analyzing the wave-grating interaction in reciprocal space, the Bloch wavevectors

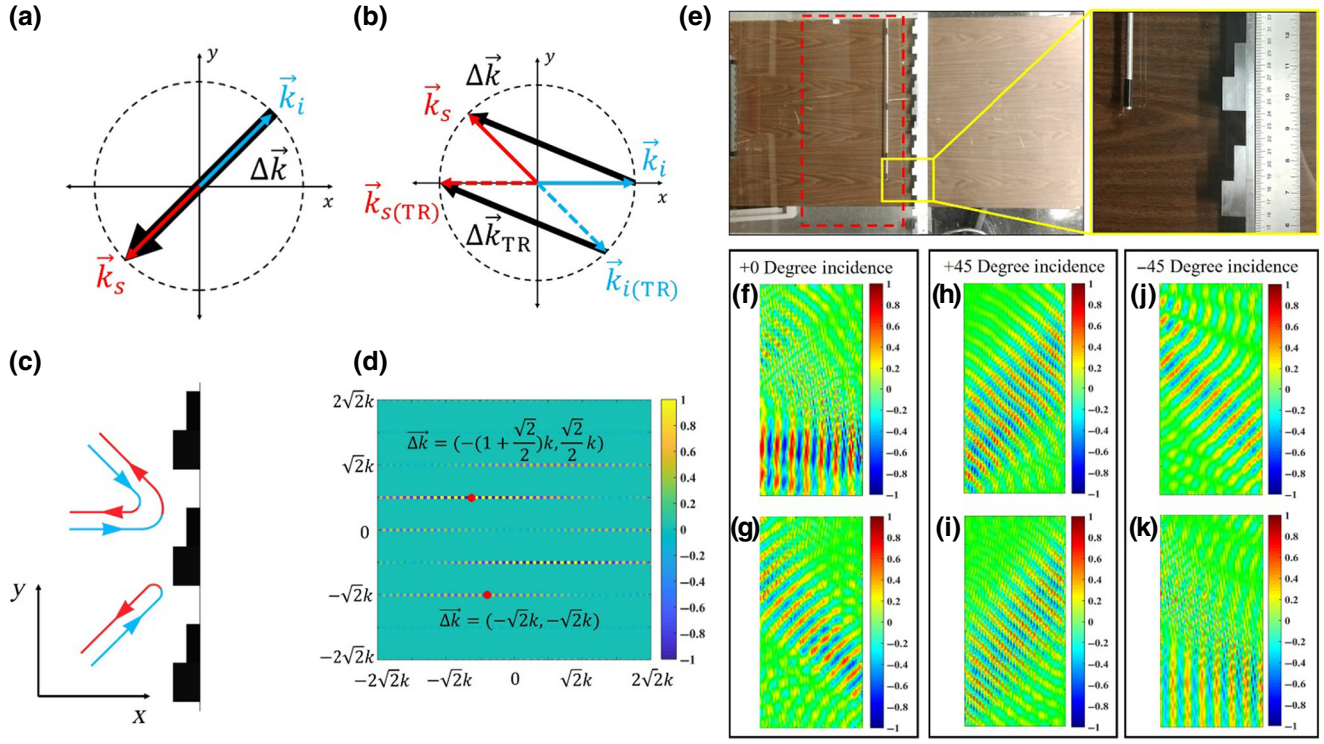

FIG. 3. (a) Wave-grating interaction for the reflection case for 45-degree incidence in the reciprocal space. (b) Wave-grating interaction for normal incidence as well as the time reversed case represented by the dashed lines. For both (a) and (b), the incident, scattered, and Bloch wavevectors are represented by $\vec{k}_i$, $\vec{k}_s$ and Δk, respectively. (c) Bianisotropic grating structure with asymmetric wave scattering in (a) and (b) determined by optimizing the unit cells using a finite element method. (d) 2D spatial Fourier transform of the grating geometry with the expected scattering wavevectors having the highest intensity to the left of the inversion symmetry about the y axis (e) Experimental set up for the bianisotropic reflection grating. The zoomed in image shows the detailed structure of the grating. The outlined rectangle with red dashed lines represents the scanned areas. (f) Measured pressure field of acoustic waves propagating with a positive k_x component for normal incidence. (g) Measured pressure field with negative k_x component for normal incidence. (h) Measured pressure field of acoustic waves propagating with positive k_x component for +45-degree incidence. (i) Measured pressure field with negative k_x component for +45-degree incidence. (j) Measured pressure field of acoustic waves propagating with positive k_x component for −45-degree incidence. (k) Measured pressure field with negative k_x component for −45-degree incidence. All the pressure fields in (f), (g), (h), (i), (j), and (k) are normalized by their corresponding maximum amplitude in each measurement.

can be determined for each incidence case. We continue to use a bianisotropic grating with linear elements where the incident and scattered wavevectors are known to remain on a circle with radius $k = 109.9\ \mathrm{m}^{-1}$ [Figs. 3(a) and 3(b)]. A wave with 45-degree incidence interacting with the bianisotropic grating results in a total reflection back toward the source requiring a Bloch wavevector of $\left(-\sqrt{2}k, -\sqrt{2}k\right)$ [Fig. 3(a)]. This Bloch wavevector is identical to that of the time reversal propagation. For normal incidence, the acoustic wave is fully reflected toward the 135-degree direction, which requires a Bloch wavevector of $\left[-\left(1+\sqrt{2}/2\right)k, \left(\sqrt{2}/2\right)k\right]$ [Fig. 3(b)]. The time reversal case for this incidence requires an identical Bloch wavevector, confirming the time reversal symmetry for both incidence cases. The asymmetric wave propagation for different incidence reveals the violation of parity symmetry about the x axis. Similar to the bianisotropic grating above, the scattered wave directions determine the grating periodicity while a finite element method is used to optimize the unit cell geometry and maximize the scattering efficiency [33]. The resulting bianisotropic grating consists of an array of scatterers having an 80.8-mm periodicity. Each scatterer consists of two rectangles: the first having a base of 18.5 mm and height of 26.5 mm directly underneath the second rectangle with a base of 9.4 mm and height of 21.2 mm [Fig. 3(c)]. Analyzing the grating geometries with spatial Fourier transform reveals the resulting Bloch wavevectors in Fig. 3(d) matching the scattering wavevectors from the symmetry analysis in Figs. 3(a) and 3(b). Inversion symmetry about the y axis can be observed in Fig. 3(d) due to the sound hard boundary behind the grating serving as a mirror to any incident pressure signals.

The designed bianisotropic grating with 13 elements is fabricated for the verification of the asymmetric wave

scattering for the reflection only case [Fig. 3(e)]. The grating elements are arranged linearly in the same waveguide described above. The speaker array is positioned in the same location for angled incidence, but is relocated to the end of the waveguide, 660 mm away from the grating for the normal incidence case. The motorized positioner scans an identical rectangular area to measure the total pressure field with both incident and scattered waves. The 2D spatial Fourier analysis mentioned above is used to separate the incident and scattered waves. Experimental measurement shows a normal incidence interacting with the bianisotropic grating results in a reflection at a 135-degree angle with reflection coefficient $R = 0.76$ [Figs. 3(f) and 3(g)]. The time reversal of this incidence is illustrated in Figs. 3(j) and 3(k) with a reflection coefficient $R = 0.88$. The 45-degree incident wave is reflected with a reflection coefficient $R = 0.84$ back toward the source [Figs. 3(h) and 3(i)]. These experimental results match with the desired scattering of the bianisotropic material in Figs. 1(e) and 1(f), whose polarizability tensor is given by Fig. 1(d). Once again, the simulations show a near perfect reflection for each incident case [33]. The unwanted wavevectors produced by the imperfect source array as well as the open boundaries at the edges of the waveguide affect the reflections in the experiment as shown in the Fourier analysis of the propagating waves [33]. The fabrication and alignment errors of the grating also contribute to the experimental error.

In conclusion, we demonstrate a systematic approach to realize an arbitrarily given bianisotropic polarizability by a designed acoustic grating. This is achieved by optimizing the geometry of the grating element to realize maximum scattering efficiency and confirming the asymmetric wave scattering of the desired bianisotropic properties in the reciprocal space through spatial Fourier analysis. The resulting parity symmetry violation of the acoustic wave propagation indicates the necessity of inversion symmetry breaking for the realization of the bianisotropic properties. The experimentally measured acoustic wave interactions with the designed bianisotropic grating match the desired scattering patterns of the given polarizability tensor. Our method paves the road for systematic realization of bianisotropic properties and asymmetric wave propagation with unitary efficiency, which is important for one-way acoustic filtering, sensing, and lensing.

ACKNOWLEDGMENTS

S.R.C. and C.S. are supported by the Georgia Tech Faculty Startup Funding. X.S. and A.N. are supported by the Office of Naval Research (ONR) MURI Program under Grant No. N0014-13-1-0631.

S.R.C. and X.S. contributed equally to this work.

[1] J. Li, L. Fok, X. Yin, G. Bartal, and X. Zhang, Experimental demonstration of an acoustic magnifying hyperlens, Nat. Mater. **8**, 931 (2009).
[2] S. J. Elliott and P. A. Nelson, Active noise control, IEEE Signal Process. Mag. **10**, 12 (1993).
[3] R.-Q. Li, B. Liang, Y. Li, W.-W. Kan, X.-Y. Zou, and J.-C. Cheng, Broadband asymmetric acoustic transmission in a gradient-index structure, Appl. Phys. Lett. **101**, 263502 (2012).
[4] H.-x. Sun, S.-q. Yuan, and S.-y. Zhang, Asymmetric acoustic transmission in multiple frequency bands, Appl. Phys. Lett. **107**, 213505 (2015).
[5] B. Liang, X. Guo, J. Tu, D. Zhang, and J. Cheng, An acoustic rectifier, Nat. Mater. **9**, 989 (2010).
[6] B.-I. Popa and S. A. Cummer, Non-reciprocal and highly nonlinear active acoustic metamaterials, Nat. Commun. **5**, 3398 (2014).
[7] R. Fleury, D. L. Sounas, C. F. Sieck, M. R. Haberman, and A. Alù, Sound isolation and giant linear nonreciprocity in a compact acoustic circulator, Science **343**, 516 (2014).
[8] D. L. Sounas, C. Caloz, and A. Alu, Giant non-reciprocity at the subwavelength scale using angular momentum-biased metamaterials, Nat. Commun. **4**, 2407 (2013).
[9] Z. Yang, F. Gao, X. Shi, X. Lin, Z. Gao, Y. Chong, and B. Zhang, Topological Acoustics, Phys. Rev. Lett. **114**, 114301 (2015).
[10] R. Fleury, A. B. Khanikaev, and A. Alu, Floquet topological insulators for sound, Nat. Commun. **7**, 11744 (2016).
[11] C. He, X. Ni, H. Ge, X.-C. Sun, Y.-B. Chen, M.-H. Lu, X.-P. Liu, and Y.-F. Chen, Acoustic topological insulator and robust one-way sound transport, Nat. Phys. **12**, 1124 (2016).
[12] J. Lu, C. Qiu, L. Ye, X. Fan, M. Ke, F. Zhang, and Z. Liu, Observation of topological valley transport of sound in sonic crystals, Nat. Phys. **13**, 369 (2017).
[13] Z. Zhang, Q. Wei, Y. Cheng, T. Zhang, D. Wu, and X. Liu, Topological Creation of Acoustic Pseudospin Multipoles in a Flow-Free Symmetry-Broken Metamaterial Lattice, Phys. Rev. Lett. **118**, 084303 (2017).
[14] M. Xiao, W.-J. Chen, W.-Y. He, and C. T. Chan, Synthetic gauge flux and Weyl points in acoustic systems, Nat. Phys. **11**, 920 (2015).
[15] J. Noh, S. Huang, D. Leykam, Y. D. Chong, K. P. Chen, and M. C. Rechtsman, Experimental observation of optical Weyl points and Fermi arc-like surface states, Nat. Phys. **13**, 611 (2017).
[16] F. Li, X. Huang, J. Lu, J. Ma, and Z. Liu, Weyl points and Fermi arcs in a chiral phononic crystal, Nat. Phys. **14**, 30 (2018).
[17] W. Zhu, X. Fang, D. Li, Y. Sun, Y. Li, Y. Jing, and H. Chen, Simultaneous Observation of a Topological Edge State and Exceptional Point in an Open and Non-Hermitian Acoustic System, Phys. Rev. Lett. **121**, 124501 (2018).
[18] X. Zhu, H. Ramezani, C. Shi, J. Zhu, and X. Zhang, PT-Symmetric Acoustics, Phys. Rev. X **4**, 031042 (2014).
[19] R. Fleury, D. Sounas, and A. Alù, An invisible acoustic sensor based on parity-time symmetry, Nat. Commun. **6**, 5905 (2015).

[20] C. Shi, M. Dubois, Y. Chen, L. Cheng, H. Ramezani, Y. Wang, and X. Zhang, Accessing the exceptional points of parity-time symmetric acoustics, Nat. Commun. **7**, 11110 (2016).

[21] G. Castaldi, S. Savoia, V. Galdi, A. Alu, and N. Engheta, in *2013 7th International Congress on Advanced Electromagnetic Materials in Microwaves and Optics (METAMATERIALS)* (IEEE, 2013), pp. 7.

[22] Y. Ra'di, D. L. Sounas, and A. Alu, Metagratings: Beyond the Limits of Graded Metasurfaces for Wave Front Control, Phys. Rev. Lett. **119**, 067404 (2017).

[23] S. A. Tretyakov and A. A. Sochava, Reflection and transmission of plane electromagnetic waves in uniaxial bianisotropic materials, Int. J. Infrared Millimeter Waves **15**, 829 (1994).

[24] C. F. Sieck, A. Alù, and M. R. Haberman, Origins of Willis coupling and acoustic bianisotropy in acoustic metamaterials through source-driven homogenization, Phys. Rev. B **96**, 104303 (2017).

[25] M. B. Muhlestein, C. F. Sieck, P. S. Wilson, and M. R. Haberman, Experimental evidence of Willis coupling in a one-dimensional effective material element, Nat. Commun. **8**, 15625 (2017).

[26] J. Li, C. Shen, A. Díaz-Rubio, S. A. Tretyakov, and S. A. Cummer, Systematic design and experimental demonstration of bianisotropic metasurfaces for scattering-free manipulation of acoustic wavefronts, Nat. Commun. **9**, 1342 (2018).

[27] L. Quan, Y. Ra'di, D. L. Sounas, and A. Alù, Maximum Willis Coupling in Acoustic Scatterers, Phys. Rev. Lett. **120**, 254301 (2018).

[28] L. Quan, D. L. Sounas, and A. Alu, Non-reciprocal willis coupling in zero-index moving media, arXiv preprint arXiv:1809.09641 (2018).

[29] D. Torrent, Acoustic anomalous reflectors based on diffraction grating engineering, Phys. Rev. B **98**, 060101 (2018).

[30] S. Koo, C. Cho, J.-h. Jeong, and N. Park, Acoustic omni meta-atom for decoupled access to all octants of a wave parameter space, Nat. Commun. **7**, 13012 (2016).

[31] B.-I. Popa, Y. Zhai, and H.-S. Kwon, Broadband sound barriers with bianisotropic metasurfaces, Nat. Commun. **9**, 5299 (2018).

[32] X. Su and A. N. Norris, Retrieval method for the bianisotropic polarizability tensor of Willis acoustic scatterers, Phys. Rev. B **98**, 174305 (2018).

[33] See Supplemental Material at http://link.aps.org/supplemental/10.1103/PhysRevApplied.11.061002 for the Fourier analysis of the wave propagation, determination of the scatterer geometries, and grating designs.